PCCP

ROYAL SOCIETY OF CHEMISTRY

PAPER

View Article Online
View Journal | View Issue

Cite this: *Phys. Chem. Chem. Phys.*, 2026, **28**, 5880

Fusion of pyrene and phenanthrene through 5*H*-imidazo[1,2-*a*]azepine scaffolds: structural tuning for fluorescence labeling and bacterial imaging

Nicholas P. Qiu, Ramin Eradeh, Liam H. Britt and Yuming Zhao *

This study investigates polycyclic aromatic fluorophores featuring pyrene and phenanthrene fused through either an imidazo[1,2-*a*]azepinone or an imidazo[1,2-*a*]azepinol central ring. These fluorophores were synthesized *via* a one-pot pyrene-4,5-dione condensation reaction and a subsequent metal hydride reduction. The molecular structures of two representative fluorophores were unequivocally determined by single-crystal X-ray diffraction (SCXRD) analysis, while their electronic absorption and emission properties were comprehensively characterized using UV-vis absorption and fluorescence spectroscopy. Excitation–emission matrix (EEM) fluorescence spectroscopy was employed to gain further insight into their emission behavior as a function of excitation energy. A combination of spectroscopic and density functional theory (DFT) studies revealed that the fluorescence behavior of azepinone-centered fluorophores is governed by a planarization-induced intramolecular charge transfer (PLICT) mechanism, resulting in pronounced solvatofluorochromism but relatively low fluorescence quantum yields. In contrast, azepinol-based fluorophores exhibited significantly higher fluorescence efficiency, albeit with much weaker solvatofluorochromic effects. To assess their potential for bioimaging applications, we investigated the interactions of these fluorophores with bovine serum albumin (BSA) as a model protein using fluorescence titration. All fluorophores bound to BSA, quenching its tryptophan fluorescence at 354 nm while emitting at their characteristic wavelengths. Detailed binding parameters were derived by fitting the data to the Stern–Volmer equation and a 1 : 1 binding isotherm. Molecular docking and molecular dynamics (MD) simulations further elucidated the fluorophore–BSA interactions at the atomic level. Finally, the fluorophores were incubated with two types of bacterial cells to evaluate their fluorescence imaging performance. The results demonstrated promising utility in optical sensing and imaging of bacteria.

Received 1st August 2025,
Accepted 23rd January 2026

DOI: 10.1039/d5cp02942b

rsc.li/pccp

Introduction

Polycyclic aromatic hydrocarbons (PAHs) are a class of rigid, highly π-delocalized molecular materials that have significant fundamental and practical importance in organic electronics and optoelectronics. Their well-defined π-conjugated frameworks enable tunable electronic and optical properties, making them ideal candidates for applications ranging from organic semiconductors to light-emitting devices.[1–3] Low-molecular-weight PAHs, such as pyrene, anthracene, and phenanthrene, are particularly notable for their high fluorescence quantum yields and microenvironment-sensitive emission. These properties have been exploited in a variety of applications, including organic light-emitting diodes (OLEDs), chemical sensors, and bioimaging probes.[4–11] The optoelectronic versatility of PAHs can be further enhanced by incorporating heterocyclic moieties (*e.g.*, imidazole, thiophene, or pyrrole), which add electron-rich or electron-deficient sites to modulate intramolecular charge transfer (ICT) and improve photostability.[12–14] Such heterocycle-integrated PAHs display unique photophysical properties, including aggregation-induced emission (AIE) for solid-state luminescence, solvatofluorochromism for microenvironment-responsive sensing, and redox-active fluorescence switching for bioimaging and chemical detection. Among these systems, phenanthroimidazole and pyrenoimidazole derivatives stand out due to their exceptional brightness, photostability, and multifunctional applicability in electroluminescent devices, ratiometric fluorescent sensors, and live-cell imaging.[15–31]

Our recent investigations have led to the serendipitous discovery of a novel class of pyrenoimidazole–phenanthrene hybrids derived from pyrene-4,5-diones directly through a one-pot reaction.[32] For instance, the compound

Department of Chemistry, Memorial University of Newfoundland, St. John's, A1C 5S7, Newfoundland and Labrador, Canada. E-mail: yuming@mun.ca; Fax: +1 709 864 3702; Tel: +1 709 864 8747

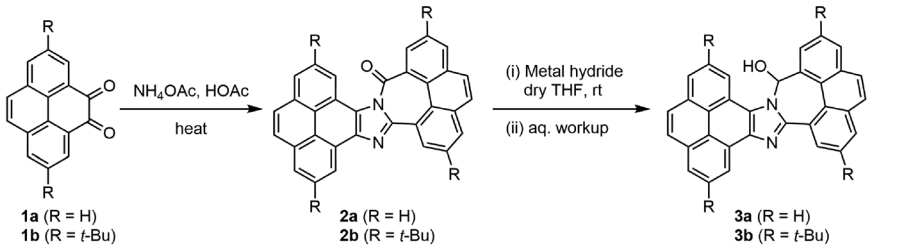

Entry	T (°C)	Time (h)	Yield (%)
2a	100	10	25
	115	48	72
2b	100	10	50
	115	12	81

Entry	Metal hydride	Time (h)	Yield (%)
3a	$LiAlH_4$	0.5	47
	BH_3·THF	1.0	39
	DIBAL-H	12	28
	$LiBH_4$	18	31
3b	$LiAlH_4$	0.5	43

Fig. 1 Optimized synthesis of pyrene–imidazoazapine–anthracene fluorophores **2** and **3**.

6*H*-phenanthro[4,5-*cde*]pyreno[4′,5′:4,5]imidazo[1,2-*a*]azepin-6-one (**2a**) can be generated through self-condensation of pyrene-4,5-dione (**1a**) in glacial acetic acid with ammonium acetate (see Fig. 1). The unique polycyclic backbone of **2a** features a π-conjugated architecture where a pyrenyl (**Py**) unit and a phenanthryl (**Phen**) unit are fused with a 5*H*-imidazo[1,2-*a*]azepin-5-one (**ImAz**) central core. Our condensation chemistry has been shown to be versatile, extending to alkylated pyrene-4,5-diones,[32,33] where the introduced alkyl groups significantly improved solubility in common organic solvents by disrupting intermolecular aggregation.

In our initial report on this type of compound, studies were focused on the synthesis and characterization of the soluble *tert*-butylated derivative (**2b**), disclosing intriguing structural and photophysical properties as well as potential application as a functional fluorophore.[32] The properties of its unsubstituted analogue (**2a**), however, were not thoroughly uncovered in our previous work due to solubility and purification challenges. Nonetheless, both **2a** and **2b** were found to exhibit large Stokes shifts and strong microenvironment-sensitive fluorescence behavior. These attributes along with easy synthesis and excellent thermal and photochemical stability position the **Py-ImAz-Phen** fluorophores as promising candidates for fluorescence-based sensing and imaging applications that target biological systems such as DNA, proteins, and cellular structures.[34–37] For practical implementation as biological fluorophores, further development must address three critical requirements: sensitivity, selectivity, and biocompatibility. This will necessitate rational structural tuning of the **Py-ImAz-Phen** scaffold, systematic study of structure–property–function relationships, and demonstration of potential in specific biological applications.

This work aims to lay a foundation for advancing **Py-ImAz-Phen**-based fluorophores by addressing two critical challenges: improving synthetic accessibility and expanding controllability over photophysical properties at the molecular level. To this end, we first optimized the one-pot condensation protocol to overcome current synthetic limitations, establishing a more cost-effective and scalable route to the **Py-ImAz-Phen** scaffold. Next, we explored a functional group interconversion approach involving controlled metal hydride reduction, as shown in Fig. 1, to transform the central azepinone moiety into an azepinol ring, while preserving the fused polycyclic backbone and modifying the π-conjugation pattern. This selective reduction reaction has a significant impact on photophysical properties. To gain insights into structure–property relationships, we characterized the **Py-ImAz-Phen** derivatives through comprehensive crystallographic and spectroscopic analyses in combination with DFT calculations. Moreover, we tested the performance of these fluorophores in protein binding and bacterial imaging. Our findings demonstrate that structural modifications of the **Py-ImAz-Phen** core can yield versatile fluorescent probes for biological labeling and imaging applications.

Results and discussion

Optimization of synthesis

The self-condensation reaction leading to the formation of the **Py-ImAz-Phen** core was optimized, through which two analogous derivatives **2a** and **2b** were obtained with markedly improved yields compared to prior reports.[32] Previously, the condensation of pyrene-4,5-dione (**1a**) with ammonium acetate in glacial acetic acid was carried out under reflux at 100 °C for 10 hours, resulting in **2a** with a yield of 25%. The self-condensation of more soluble 2,7-di-*tert*-butylpyrene-4,5-dione (**1b**) under the same conditions afforded **2b** in a higher yield of 50%. In this work, the yields of **2a** and **2b** were improved through modified reaction conditions and workup procedures. Under our initial conditions of refluxing **1a** at 100 °C for 10 hours, the starting material **1a** was not completely consumed. We therefore investigated conditions with increased reaction time and temperature. After numerous trials, the yield of **2a** was significantly increased to 72% under the conditions of refluxing at 115 °C for 48 hours. Elongation of the reaction time beyond 48 hours resulted in lowered yields, as more byproducts were formed with increasing time. Similarly, we optimized the synthesis of **2b** through tuning the reaction time and temperature. The condensation of **1b** at 115 °C for 12 hours was found to end with complete consumption of the starting

material, affording the condensation product **2b** in a high yield of 81%. Compared with the conditions for synthesizing **2a**, the reaction time was much shorter. The better solubility of 2,7-di-*tert*-butylpyrene-4,5-dione (**1b**) in the solution phase is believed to be a key reason for the faster reaction rate. The molecular structures of **2a** and **2b** were convincingly determined using NMR and MS analyses (see the SI for details), which are consistent with those previously reported.[32]

Compounds **2a** and **2b** were next subjected to a metal hydride reduction reaction. While typical metal hydride reduction of amides leads to amine products, the reduction of **2a** and **2b** had their amide groups converted into hemiaminals, affording azepinol derivatives **3a** and **3b**, respectively. To probe the reaction scope and improve reaction yields, we tested different metal hydrides as the reducing reagents, including $LiAlH_4$, BH_3·THF, DIBAL-H, and $LiBH_4$. The synthetic outcomes are summarized in the table given in Fig. 1. Reduction of **2a** with $LiAlH_4$ was found to exhibit the highest yields. Actually, $LiAlH_4$ was the only reducing reagent that led to the complete consumption of the starting material. Eventually, the reduction conditions of **2a** were optimized as follows: reacting **2a** with $LiAlH_4$ in dry THF under a nitrogen atmosphere for 30 minutes, followed by aqueous workup and silica column chromatographic purification, resulting in **3a** with a yield of 47%. A similar procedure was applied to the reduction of **2b**, leading to the formation of **3b** in 43% yield. After the synthesis, the structures of compounds **3a** and **3b** were confirmed by NMR and MS characterization (see the SI for details). Both **3a** and **3b** show better solubility, especially in polar organic solvents, than their azepinione-based precursors **2a** and **2b**.

Single-crystal structure analysis

Single crystals of **2a** and **3a** were grown through slow evaporation of their THF solutions at room temperature. With them, SCXRD analysis was conducted to elucidate their molecular structures and packing motifs in the crystalline state. As shown in Fig. 2A, azepinone-centered **2a** adopts a nearly planar conformation except the C═O group on the azepinone ring. The interplanar angle between the pyrene and phenanthrene moieties is only 3.4°, yielding a flat π-framework in favor of slipped π-stacking in the crystal structure. The packing diagram of **2a** (Fig. 2C) shows an organized herringbone-type stacking motif, which is commonly seen in the crystal packing of planar PAH molecules.[38–40]

The imidazolyl unit of **2a** possesses Lewis basicity, allowing for coordination with Lewis acids such as tris(pentafluorophenyl)borane (BARF) hydrate. The acid–base complex resulting from this interaction was carefully crystallized in THF at room temperature. X-ray structural analysis showed that one of the imidazolyl nitrogen atoms of **2a** was protonated (see Fig. 2B). The resulting imidazolium ion subsequently formed a hydrogen bond with the oxygen atom of BARF. The **2a**–BARF complex possesses much better solubility than **2a** itself. This is due to the conformation of **2a** being significantly twisted after complexation with bulky BARF. Upon complexation, the pyrene and phenanthrene units of **2a** adopt an interplanar angle of 41.7°, which is far greater than that of pristine **2a**. This distorted conformation hinders intermolecular π-stacking (see Fig. 2D) and hence improves solubility.

The X-ray structure of **3a** displays a significantly distorted conformation due to the presence of an sp^3 hybridized carbon in the central azepinol ring (Fig. 3A). Specifically, the angle

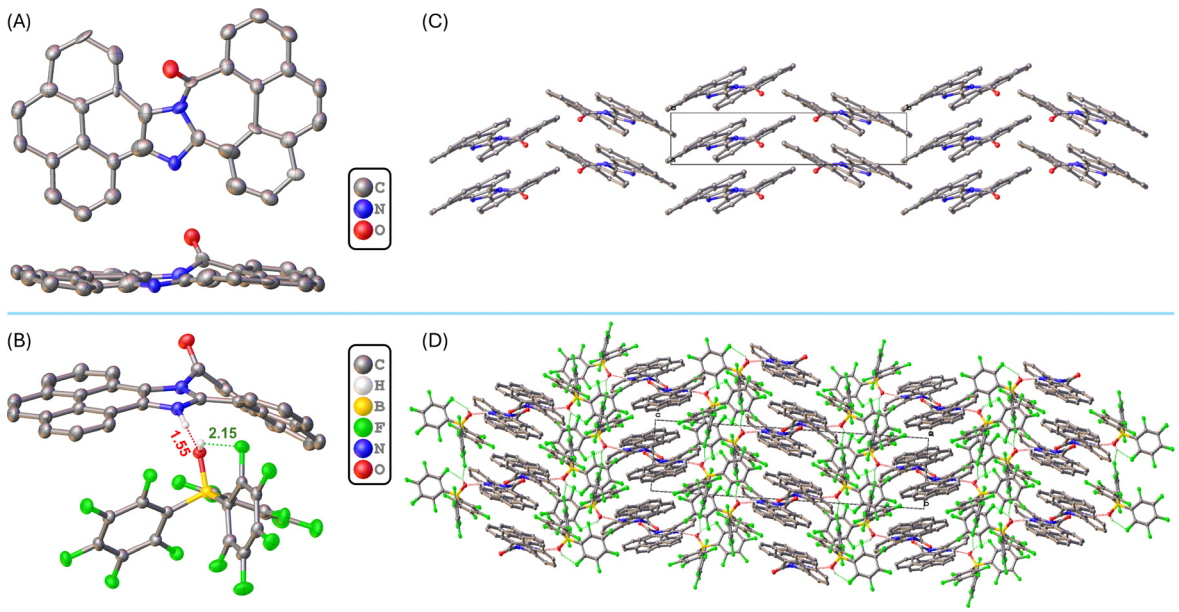

Fig. 2 (A) X-Ray structure of **2a** viewed from different perspectives (with thermal ellipsoids drawn at 50% probability and hydrogen atoms omitted; CCDC 2256234). (B) X-Ray structure of the 1:1 complex of **2a** and BARF viewed from different perspectives (with thermal ellipsoids drawn at 50% probability and hydrogen atoms omitted; CCDC 2430322). (C) Crystal packing diagram of **2a**. (D) Crystal packing diagram of the **2a**–BARF complex.

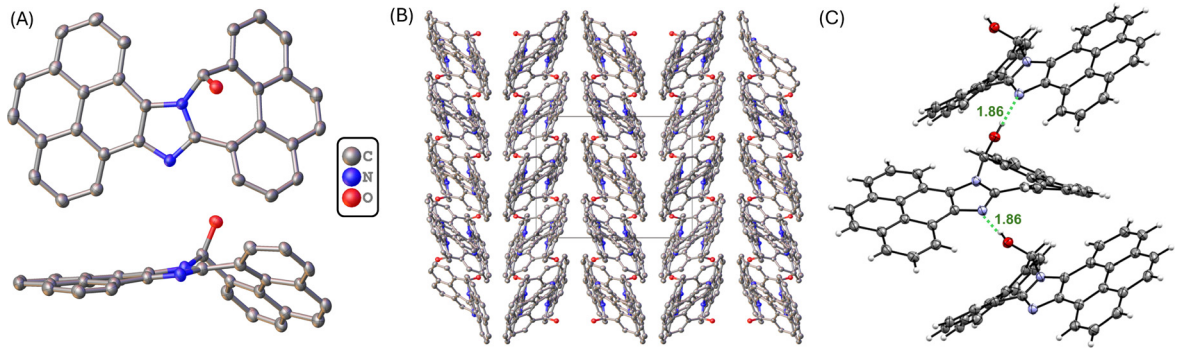

Fig. 3 (A) X-ray structure of **3a** viewed from different perspectives (with thermal ellipsoids drawn at 50% probability and hydrogen atoms omitted; CCDC 2430295). (B) Crystal packing diagram of **3a**. (C) Intermolecular hydrogen bonding interactions in the crystal structure of **3a**.

between the pyrene and phenanthrene planes is 37.1°, which is significantly greater than that of **2a**. The degree of π-conjugation across the molecule of **3a** is therefore reduced, resulting in its markedly distinct photophysical properties in comparison with **2a** (*vide infra*). The crystal packing of **3a** (see Fig. 3B) exhibits two key organizational features: (i) local ordering through slipped π-stacking interactions between pyrene units of adjacent molecules (interplanar distance = 3.35 Å) and (ii) long-range organization of supramolecular networks assembled *via* hydrogen bonding interactions between hydroxy groups and imidazolyl nitrogen atoms (OH···N distance = 1.86 Å, O···N distance = 2.75 Å, and O–H···N angle = 175.0°). The combined effects of π-stacking and hydrogen bonding generate a hierarchical supramolecular architecture, where π-stacking creates molecular dimers that further assemble into extended networks through hydrogen bonding. As illustrated in Fig. 3C, the hydroxy group (H-bond donor) engages with one of the imidazolyl nitrogen atoms (H-bond acceptor) to form an intermolecular hydrogen bond, with the H···N distance being 1.86 Å.

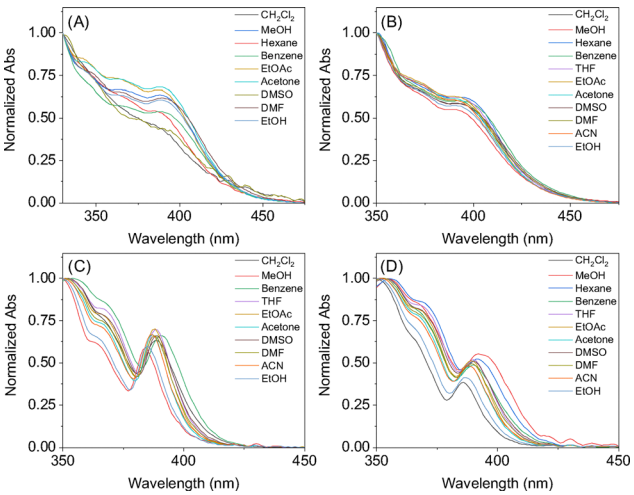

Fig. 4 Normalized UV-vis spectra of compounds (A) **2a** (1.0×10^{-4} M), (B) **2b** (1.0×10^{-4} M), (C) **3a** (1.5×10^{-5} M) and (D) **3b** (1.5×10^{-5} M) in various organic solvents.

Solution-phase electronic absorption properties

The electronic properties of compounds **2** and **3** were investigated using UV-vis absorption spectroscopy in solvents of varying polarity (Fig. 4). Compound **2a** shows characteristic π → π* transition bands that remain largely invariant across different solvent environments. Notably, the lowest-energy absorption band exhibits minimal spectral shifts ($\Delta\lambda$ < 3 nm) between nonpolar and polar solvents (Fig. 4A), demonstrating negligible solvatochromic behavior in the ground state. Significant variations in relative absorbance intensities were observed, which did not correlate with solvent polarity. It appears that the UV-vis absorption characteristics of **2a** are primarily influenced by solubility-dependent aggregation effects rather than dielectric interactions with solvents.

The UV-vis data of compound **2b** also show relatively weak solvatochromism across all solvents examined (Fig. 4B). A systematic analysis, however, reveals a subtle degree of polarity dependence; that is, polar solvents (MeOH, EtOH, DMF, and DMSO) induce small hypsochromic shifts by *ca.* 2–3 nm, while nonpolar solvents (hexane and benzene) cause slight bathochromic shifts of 7–8 nm. This pattern establishes a weak but measurable correlation with solvent polarity parameters. Different from **2a**, the intensity of the low-energy absorption band in the normalized spectra of **2b** changes in a much smaller degree across different solvents, which can be attributed to the effect of enhanced solubility conferred by the *tert*-butyl substituents. It is noteworthy that the UV-vis absorption energies of **2a** and **2b** do not show a significant dependence on the solvent environment, attesting to the robustness of their **Py-ImAz-Phen** core in retaining its vertical electronic transition properties regardless of the solvent effect.

Azepinol derivatives **3a** and **3b** exhibit notable solvatochromism as evidenced by their varying UV-vis profiles in different solvents (Fig. 4C and D). For compound **3a**, the π → π* transition displays a bathochromic shift from nonpolar to polar aprotic solvents (*e.g.*, 388 nm in CH_2Cl_2 to 398 nm in DMF), while alcohol solvents induce an anomalous hypsochromic shift (385 nm in ethanol and 384 nm in methanol). This unusual behavior likely arises from a combined effect of

reduced solubility and enhanced aggregation in protic solvents. It is also worth noting that the absorption bands of **3a** are consistently hypsochromically shifted by 5–10 nm relative to its planar counterpart **2a**, as a result of its twisted conformation (*i.e.*, decreased π-conjugation degree).

The solvatochromic effects are most pronounced for the *tert*-butyl derivative **3b**, which exhibits a wider range of spectral shifts from 381 nm in CH_2Cl_2 to 393 nm in methanol (Fig. 4D). These variations lack correlation with conventional solvent polarity scales, suggesting complex interplays between the molecular structure and solvation effects in governing the electronic absorption properties of these azepinol-containing systems.

Solvatofluorochromic effects

Fluorescence spectroscopic analysis of fluorophores **2a/b** and **3a/b** was conducted in different organic solvents. As illustrated in Fig. 5A, compound **2a** exhibits the most pronounced solvatofluorochromic effect among the four fluorophores, with emission maxima (λ_{em}) changing from 439 nm (in methanol) to 543 nm (in CH_2Cl_2). In the most polar solvent, DMSO, fluorophore **2a** emits at a λ_{em} of 533 nm. The observed λ_{em} values of **2a** show no clear correlation with solvent polarity, suggesting that the solvatofluorochromism of **2a** is dependent on multiple solvent factors rather than polarity. To quantitatively understand the effect of solvent polarity, the Lippert–Mataga plot[41,42] was utilized to assess the correlation between the Stokes shift (ν_{SS}) and solvent polarity. The equation is expressed as follows:

$$\nu_{SS} = \frac{2(\mu_e - \mu_g)^2}{hca^3}\left(\frac{\varepsilon - 1}{2\varepsilon + 1} - \frac{n^2 - 1}{2n^2 + 1}\right) + C$$

where μ_e and μ_g are the dipole moments of the solute in the excited and ground states, respectively, h is Planck's constant, c is the speed of light, a is the Onsager cavity radius of the solute molecule, and C is a constant. The term in parentheses, known as the orientation polarizability (Δf) of the solvent, quantifies how the solvent environment stabilizes the electronic states of the solute. As shown in Fig. 6, the data points of **2a** scatter widely and completely lack linear correlation. This analysis corroborates the point established above in a quantitative way; the solvatofluorochromism of **2a** is not exclusively dependent on solvent polarity. Solubility and intermolecular aggregation likely exert a significant influence as well, further complicating the solvatofluorochromic behavior of **2a**.

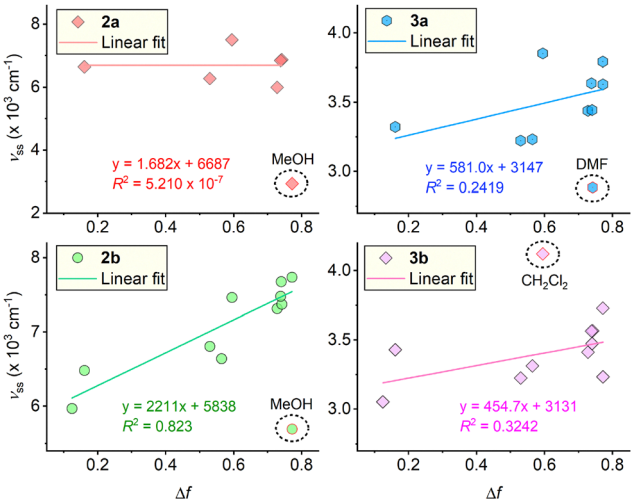

Fig. 6 Lippert–Mataga plots of fluorophores **2a/b** and **3a/b**. Data points indicated by dashed circles are excluded from linear fitting analysis due to considerable deviation.

As can be seen from Fig. 5B, fluorophore **2b** exhibits emission maxima ranging from 501 nm in methanol to 555 nm in DMSO. Although the range of this spectral shift is narrower than that observed for **2a** (439–543 nm), it remains sufficiently large to produce visually discernible color changes upon variation of solvent polarity (Fig. 7). In contrast to its unsubstituted analogue **2a**, the solvatofluorochromic behavior of **2b** complies well with the Lippert–Mataga equation. Fig. 6 demonstrates a linear relationship between the Stokes shift of **2b** and the solvent polarity parameter Δf, while the slope of the plot is the greatest of the fluorphores examined. According to the Lippert–Mataga equation, this outcome indicates a large difference between the dipole moments in the ground and excited state, hence suggesting a strong ICT characteristic of the

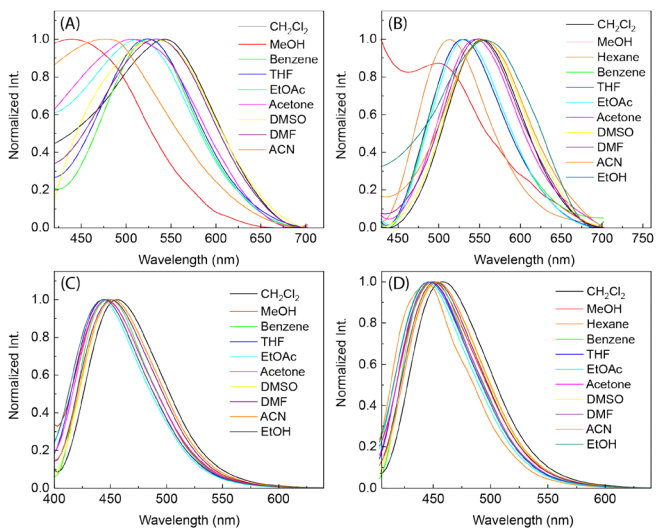

Fig. 5 Normalized fluorescence spectra of (A) **2a** (1.0 × 10^{-4} M), (B) **2b** (1.0 × 10^{-4} M), (C) **3a** (1.5 × 10^{-5} M) and (D) **3b** (1.5 × 10^{-5} M) in various organic solvents.

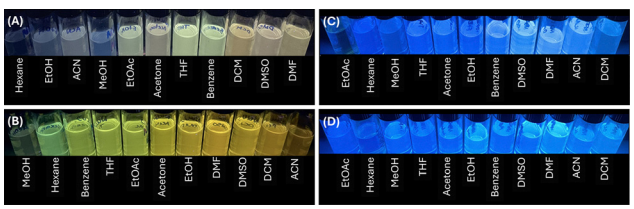

Fig. 7 Photographic images of the solutions of (A) **2a** (1.0 × 10^{-4} M), (B) **2b** (1.0 × 10^{-4} M), (C) **3a** (1.5 × 10^{-5} M) and (D) **3b** (1.5 × 10^{-5} M) in various organic solvents under the irradiation of a UV lamp (λ_{ex} = 254 nm).

fluorescence. Given the significant steric effect of *tert*-butyl substituents, intermolecular π-stacking and aggregation can be ruled out as key players in the fluorescence mechanism of **2b**. The well-behaved Lippert–Mataga correlation of **2b** therefore reflects the effects of solvent polarity on the photophysical characteristics of individual **Py-ImAz-Phen** molecules. It is also worth noting that methanol appears as an outlier in the solvent-dependent analysis of both **2a** and **2b**, suggesting that alcohols give more complex solvation effects (*e.g.*, hydrogen bonding) than other organic solvents do.

The fluorescence spectra of azepinol-based fluorophores **3a** and **3b** exhibit much weaker degrees of solvatofluorochromism than azepinone-based **2a** and **2b** do. As shown in Fig. 5C and D, the emission maxima vary from *ca.* 444 to 460 nm in different solvents. The most redshifted emission was observed in CH_2Cl_2 (457 nm for **3a** and 460 nm for **3b**). Their Lippert–Mataga analysis shows significantly scattered data points and low degrees of linear correlation (Fig. 6). Although some linear trends can be inferred based on these data, the slopes of the linear fitting plots of **3a** and **3b** are much smaller than that observed for **2b**. These results confirm that introduction of an sp^3 carbon in the central azepinol ring reduces the electronic communication between the pyrene and phenanthrene units and consequently eliminates ICT as an effective mechanism for the photophysics of **3a** and **3b**. As such, the fluorescence emission of **3a** and **3b** is not very sensitive to the solvent environment. Visually, both fluorophores exhibit blue fluorescence color in different solvents, contrasting the strong solvatofluorochromism of **2a** and **2b** (Fig. 7).

Fluorescence quantum yields and lifetimes

The fluorescence quantum yields (Φ_f) and lifetimes (τ) of **2a/b** and **3a/b** were measured in dilute DMF solutions, with detailed data summarized in Table 1. The azepinone-based fluorophore **2a** exhibits weak fluorescence, characterized by a low quantum yield (Φ_f = 0.132). The fluorescence efficiency of its *tert*-butyl-substituted analogue **2b** is even lower (Φ_f = 0.082). Given that the bulky *tert*-butyl group can effectively suppress intermolecular aggregation in solution, the effect of aggregation-caused quenching (ACQ) can be ruled out as a reason for the low Φ_f values of both **2a** and **2b**. Rather, the ICT nature of the π-conjugated framework of **Py-ImAz-Phen** in the first excited (S_1) state could more reasonably explain their low fluorescence efficiency. As shown in Fig. 8A, the TD-DFT optimized geometry of **2a** in the first excited (S_1) state exhibits a more co-planar arrangement of the phenanthrene and pyrene units than its ground (S_0) state does. This conformational change results in the S_1 state being more polar than the S_0 state by 0.51 Debye, signifying a planarized intramolecular charge transfer (PLICT) characteristic for the S_1 state.[43–46] Emission through an ICT state typically features low-to-moderate quantum yield due to competitive non-radiative decay pathways.

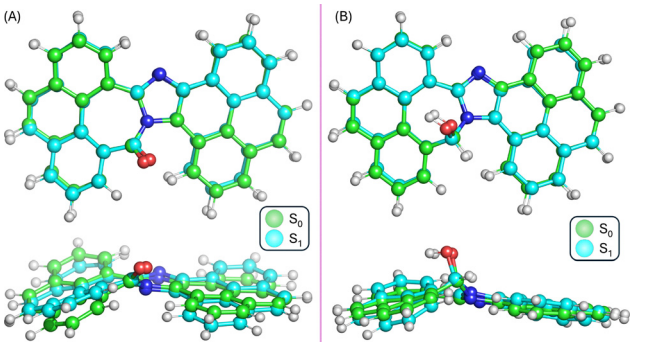

Fig. 8 Ball-and-stick models comparing the optimized geometries of (A) **2a** and (B) **3a** in the S_0 (carbon atoms highlighted in green color) and S_1 states (carbon atoms highlighted in cyan color). Calculations were performed at the PCM(DMF)//(TD)M06-2X/DEF2SVP level of theory.

In contrast to **2a/b**, azepinol-based fluorophores **3a** and **3b** display much higher fluorescence quantum yields, which are Φ_f = 0.679 and 0.816, respectively. The presence of an sp^3-hybridized carbon in the azepinol ring disrupts π-conjugation and increases the degree of structural distortion (*vide supra*), markedly reducing the propensity for ICT state formation. The fluorescence of **3a/b** hence results from a localized excited (LE) state rather than an ICT state. (TD)DFT calculations showed that the S_1 state of **3a** is more twisted than its S_0 state (see Fig. 8B), which is different from the case of **2a**. In particular, the dipole moments of **3a** in the S_0 and S_1 states differ by merely 0.04 Debye, confirming minimal charge redistribution involved in the $S_0 \rightarrow S_1$ transition.

The differences between the lowest excited (S_1) states of **2a** and **3a** can be intuitively obtained by natural transition orbital (NTO) analysis[47] (see Fig. 9). For fluorophore **2a**, the particle distribution is mainly located on the pyrene and imidazole units, while the hole distribution significantly shifts to the segment around the C═O unit of the azepinone ring and the adjacent phenyl ring of the phenanthryl group. For fluorophore **3a**, the particle and hole distributions are in similar areas within the molecule, encompassing pyrene, imidazole, and phenanthrene groups. The NTO analysis indicates that the S_1 state of **2a** possesses a more pronounced ICT characteristic than that of **3a**.

Table 1 Summary of fluorescence quantum yields (Φ_f) and lifetimes (τ) of **2a** (7.5×10^{-4} M), **2b** (5.0×10^{-4} M), **3a** (8.1×10^{-4} M), and **3b** (5.0×10^{-4} M) measured in DMF at room temperature

Entry	Φ_f	τ_1 (ns)	Weight % τ_1	τ_2 (ns)	Weight % τ_2	χ^2
2a	0.132	0.64 ± 0.01	82.8 ± 1.0%	4.53 ± 0.02	17.2 ± 0.02%	1.123
2b	0.082	0.80 ± 0.01	99.1 ± 0.50%	3.56 ± 0.21	0.90 ± 0.13%	1.079
3a	0.679	4.05 ± 0.005	100 ± 0.14%	—	—	1.109
3b	0.816	4.11 ± 0.005	100 ± 0.14%	—	—	1.257

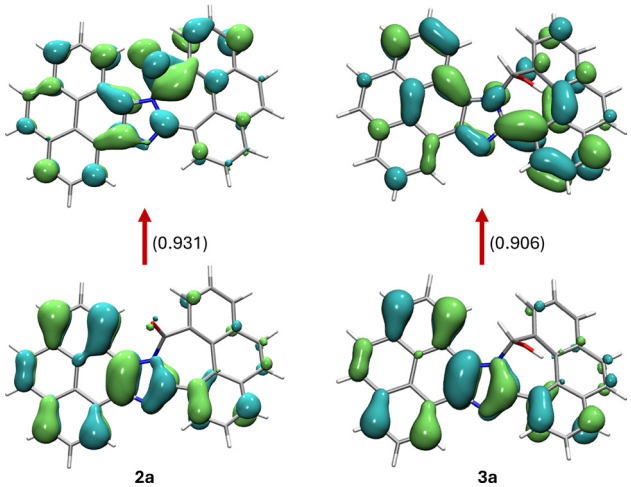

Fig. 9 Natural transition orbitals (NTOs) characterizing the S_1 states of **2a** and **3a** in DMF. The weights obtained by NTO analysis are shown in parentheses and the isovalue for the contour plots is 0.03 a.u.

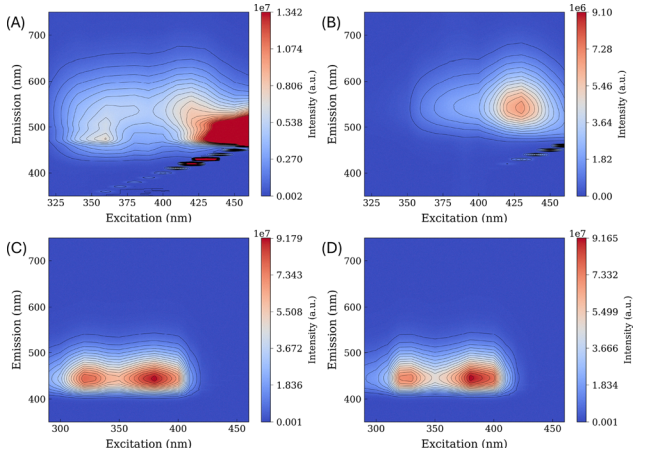

Fig. 10 EEM contour plots of (A) **2a** (7.5×10^{-4} M), (B) **2b** (5.0×10^{-4} M), (C) **3a** (8.1×10^{-4} M) and (D) **3b** (5.0×10^{-4} M) measured in DMF at room temperature.

The fluorescence decay kinetics of **2a** was determined to comply with a bi-exponential model, yielding two distinct lifetimes of 0.64 ns and 4.53 ns (see Table 1). A similar bi-exponential decay was observed for **2b**, with lifetimes of 0.80 ns and 3.56 ns, respectively. The absence of dual emission bands in the steady-state fluorescence spectra of **2a** and **2b** suggests that both emissive states are of similar energies despite their different lifetimes. The shorter lifetime component can be attributed to a more rigid, planar conformation based on comparative analysis of the **2a**–BARF complex. This complex shows three lifetimes, with the shortest one (0.21 ns) giving a contribution of 56.5% (see Table S-4 and Fig. S-6 in the SI). As X-ray crystallographic data have disclosed a more twisted molecular conformation of **2a** in the complex, the reduced contribution of the short lifetime can be reasonably linked to lowered population of a more planarized excited state(s).

The fluorescence decays of compounds **3a** and **3b** both follow a mono-exponential mechanism, showing lifetimes of 4.05 ns (**3a**) and 4.11 ns (**3b**), respectively. The results manifest that the fluorescence mechanisms of **3a** and **3b** are governed by only one emissive excited state. As disclosed by TD-DFT analysis, the S_1 states of **3a** and **3b** are more twisted than their ground states, hence prolonging their fluorescence lifetimes in comparison with the major lifetimes observed for **2a** and **2b**.

Excitation–emission matrix (EEM) analysis

Fluorophores **2a/b** and **3a/b** were subjected to excitation–emission matrix (EEM) analysis to gain deeper insights into the distinct photophysical behaviors arising from their different π-frameworks as well as the effect of peripheral substitution (see Fig. 10). EEM contour plots of **2a** and **2b** reveal intense emission signals when excited at wavelengths ≥425 nm (Fig. 10A and B), coinciding with the lowest-energy absorption bands (*i.e.*, $S_0 \rightarrow S_1$ transition) in their UV-vis spectra. Interestingly, **2a** exhibits maximal emission intensity upon excitation beyond 450 nm, a spectral region where its ground-state absorptivity is very low. In contrast, the EEM plot of compound **2b** only displays a prominent emission "blob" that encompasses a narrow region of excitation wavelengths centering around 425 nm. When the excitation wavelength surpasses 450 nm, the emission intensity diminishes. The different EEM patterns between **2a** and **2b** can be ascribed to the absence/presence of peripheral *tert*-butyl groups on the **Py-ImAz-Phen** core. The unsubstituted **2a** favors the formation of intermolecular π-stacked assemblies in the solution phase (*e.g.*, π-dimer or oligomers). Such assemblies would absorb lower energy than the individual molecules do, and this proposed model was supported by concentration-dependent UV-vis experiments (see Fig. S-7A, SI). It is therefore reasonable to propose that photoexcitation of the π-stacked assemblies of **2a** leads to the formation of an excited complex, which quickly dissociated into individually excited monomers, leading to fluorescence (Fig. 11A). For **2b**, the steric effects of *tert*-butyl groups hinder intermolecular π-stacking. As such, the EEM plot only reflects the characteristic excitation–emission relationships of the individualized **Py-ImAz-Phen** core, without being convoluted with aggregation-induced mechanisms.

The EEM profiles of azepinol-based fluorophores **3a** and **3b** share a similar feature; that is, excitation at both 320 nm and

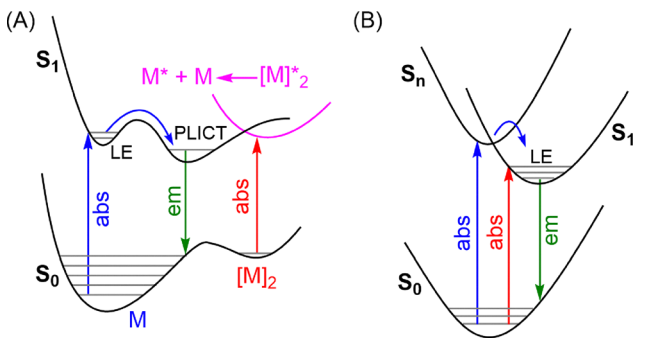

Fig. 11 Proposed photophysical mechanisms for the excitation–emission properties of (A) **2a** and (B) **3a/b**.

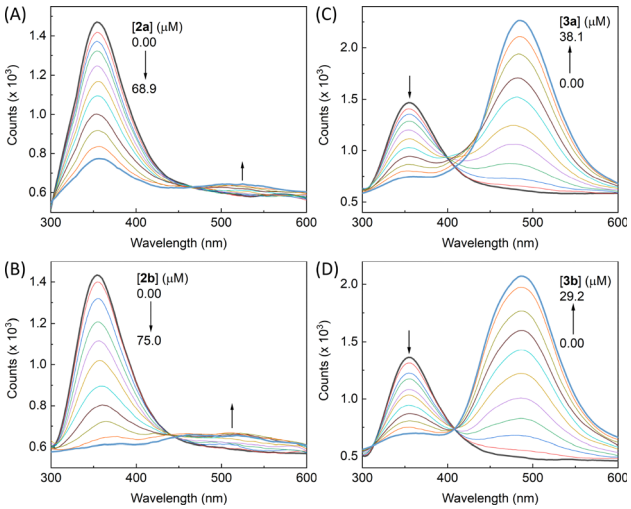

Fig. 12 Fluorescence spectra tracking the titration of bovine serum albumin (10 μM) with (A) **2a**, (B) **2b**, (C) **3a**, and (D) **3b** in 0.1 M phosphate buffer (pH 7.4). Excitation wavelength (λ_{ex}): 277 nm. Arrows denote spectral changes with increasing fluorophore concentration.

390 nm generates emission bands with nearly identical spectral ranges and maxima (Fig. 10C and D). When excited at 390 nm, **3a** is directly promoted to its first singlet excited (S_1) state, which decays radiatively to produce fluorescence. In contrast, 320 nm excitation primarily accesses a higher-lying excited state, likely stemming from excitation of the phenanthrene chromophore. The resulting excited state (S_n) then undergoes facile internal conversion (IC) to relax the system to the emissive S_1 state, which yields fluorescence at wavelengths characteristic of pyrenoimidazole (420–480 nm).[48] Despite the disruptive effect of the sp^3-hybridized carbon in the azepinol ring on π-conjugation, the phenanthrene and pyrene chromophores remain sufficiently coupled to enable energy funneling from phenanthrene to pyrene (Fig. 11B).

Interactions with bovine serum albumin

The binding affinities and interaction mechanisms of our four fluorophores with bovine serum albumin (BSA) were investigated using fluorescence titration experiments. BSA was selected as a benchmark protein for this study due to the following reasons. First, BSA is a widely used model protein for the most abundant protein constituent (52–62%) in the water-soluble fraction of blood plasma. Second, its well-characterized structure and binding properties make it a reliable model protein for studying biomolecular interactions.[49] Third, the extensive literature on BSA binding to various chemical species[50] allows for meaningful comparison with the results obtained in this study. BSA consists of a single polypeptide chain of 583 amino acid residues.[51] The presence of two tryptophan (Trp) residues, specifically Trp-134 and Trp-212, gives rise to a characteristic fluorescence emission band around 354 nm,[52] facilitating detailed examination of ligand–BSA binding properties by fluorescence spectroscopy.

In our experimental analysis, BSA (1.0×10^{-5} M) in a phosphate buffer solution (pH 7.4) was subjected to progressive addition of fluorophores **2a**, **2b**, **3a**, and **3b**, respectively. As shown in Fig. 12, all fluorophores induced concentration-dependent quenching of BSA's intrinsic fluorescence, indicating the formation of ground-state complexes between the fluorophores and BSA. The quenching data were quantified using the Stern–Volmer equation:

$$\frac{F_0}{F} = 1 + K_{sv}[Q] \quad (1)$$

where F_0 is the initial fluorescence intensity of BSA, F is the fluorescence intensity in the presence of quencher (Q), K_{sv} is the Stern–Volmer quenching constant, and [Q] is the quencher (fluorophore) concentration. The calculated K_{sv} values are summarized in Table 2.

Notably, all Stern–Volmer plots for the four fluorophores show significant deviation from linearity, exhibiting downward-curved nonlinear trends (see Fig. S-17 and S-18, SI). This behavior likely arises from either heterogeneous fluorophore populations or multiple-site binding with different affinities. To further investigate these possibilities, we employed a modified double-logarithmic model:

$$\log\left(\frac{F_0}{F} - 1\right) = \log K_b + n \log[Q] \quad (2)$$

where K_b represents the binding constant for the fluorophore–BSA interaction and n denotes the number of binding sites per fluorophore molecule.[53]

Fig. 13A–D presents the double-logarithmic plots for BSA binding with the four fluorophores. Notably, the fitting results showed satisfactory correlation coefficients (R^2 = 0.972–0.999). The calculated binding constants (K_b, Table 2) were significantly lower than those obtained from the linear Stern–Volmer analysis. The binding site values (n = 0.6–0.8) suggest heterogeneous quenching of BSA's tryptophan residues by the fluorophores.

The fluorescence titration spectra of azepinone-centered fluorophores **2a** and **2b** revealed a small but consistent enhancement in the 450–600 nm region (Fig. 12A and B). A weak, broad emission band centered at 525 nm emerged progressively during titration, attributable to the characteristic

Table 2 Summary of fluorophore–BSA binding properties determined from fluorescence titration experiments and molecular docking analysis

Entry	K_b (mol^{-1} L)	n	K_{SV} (mol^{-1} L)	K_d^{obs} (mol L^{-1})	E_b^{cald} (kcal mol^{-1})	K_d^{cald} (mol L^{-1})
2a	4.79×10^2	0.657	1.45×10^4	4.82×10^{-5}	10.39	2.41×10^{-8}
2b	4.28×10^3	0.815	2.22×10^4	1.47×10^{-5}	9.55	9.91×10^{-8}
3a	8.71×10^2	0.667	2.90×10^4	2.01×10^{-5}	9.94	5.21×10^{-8}
3b	2.91×10^3	0.762	3.68×10^4	1.65×10^{-5}	9.03	2.42×10^{-7}

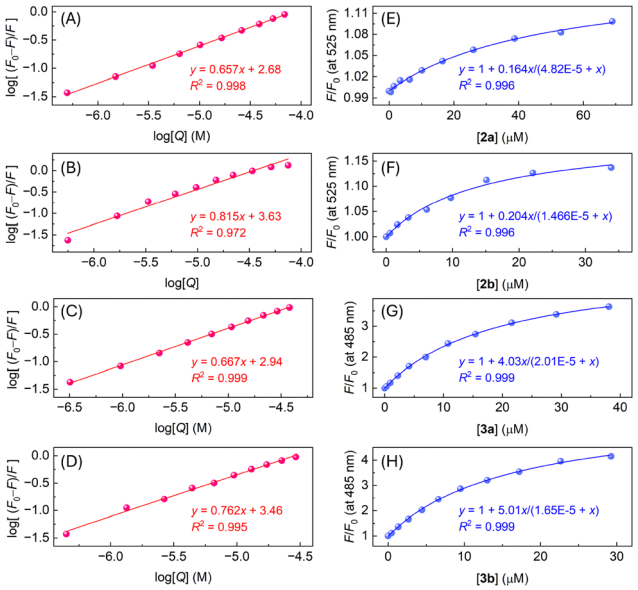

Fig. 13 Fluorescence titration data for compounds **2a** (A), **2b** (B), **3a** (C), and **3b** (D) fitted to the double-logarithmic model (eqn (2)). Fluorescence titration data for compounds **2a** (E), **2b** (F), **3a** (G), and **3b** (H) fitted to a 1 : 1 binding isotherm (eqn (3)).

PLICT emission of **Py-ImAz-Phen**. The fluorescence enhancement (F/F_0) can be correlated with the fluorophore concentration ([Q]) using a 1 : 1 binding isotherm:

$$\frac{F}{F_0} = 1 + \frac{\Delta F_{max}[Q]}{K_d^{obs} + [Q]} \quad (3)$$

where ΔF_{max} represents the maximum change in fluorescence and K_d^{obs} is the dissociation constant for the fluorophore–BSA complex.[54] As shown in Fig. 13E and F, the binding isotherms for BSA complexation with **2a** and **2b** exhibit excellent fitting quality (R^2 = 0.996). The observed dissociation constants (K_d^{obs}), listed in Table 2, are lower than those derived from the Stern–Volmer quenching analysis by more than one order of magnitude, indicating significantly stronger binding affinities than that suggested by the quenching data alone.

The titration of BSA with azepinol-centered fluorophores **3a** and **3b** exhibited similar fluorescence quenching at 354 nm (Fig. 12C and D). In the meantime, a strong emission band emerged at 485 nm in the long-wavelength region, matching the characteristic emission of free **3a**/**b**. Compared to their azepinone analogues (**2a** and **2b**), the titrations of BSA with **3a** and **3b** resulted in much stronger emission enhancement in this long-wavelength region. EEM analysis revealed fluorescence maxima at 330 nm for **3a** and **3b**, which overlap with BSA's emission peak around 354 nm. This spectral overlap suggests a Förster resonance energy transfer (FRET) mechanism[55,56] as follows: the excitation wavelength (at 277 nm) used in the fluorescence titration measurements leads to excitation of the tryptophan residues of BSA, which subsequently transfers energy to trigger the excitation and emission of the fluorophore (at 485 nm) bound to BSA. It is worth noting that fluorophores **3a** and **3b** showed negligible fluorescence when placed in the phosphate buffer solution, due to their insolubility in aqueous media. The fluorescence enhancement around 485 nm therefore results from fluorophores bound to BSA, offering a selective fluorescence "turn-on" performance for labeling of BSA and proteins alike.[57]

Molecular docking studies

To elucidate the molecular interactions between BSA and the **Py-ImAz-Phen** fluorophores, we performed docking simulations using the VINA[58] module implemented in the YASARA software package.[59] Chain A of BSA (PDB: 4F5S) served as the receptor, with fluorophores **2a**/**b** and **3a**/**b** as ligands. Fig. 14 displays the highest-scoring binding poses and corresponding 2D interaction diagrams.

For the complex of **2a** and BSA, the carbonyl group located on the central azepinone ring of **2a** forms a hydrogen bond with His105. The pyrene moiety participates in alkyl–π stacking with Lys465 and Glu464, respectively. Fluorophore **2b** engages with BSA *via* alkyl–π (Tyr400 and Lys520) and alkyl–alkyl (Met547 and Val554) interactions. In contrast to the case of **2a**, there are no hydrogen bonding interactions between **2b** and BSA. The binding energies (E_b) calculated from the docking analysis are 10.39 kcal mol^{-1} for **2a** and 9.55 kcal mol^{-1} for **2b**. These energies correspond to dissociation constants that are considerably greater than the experimentally determined affinities by

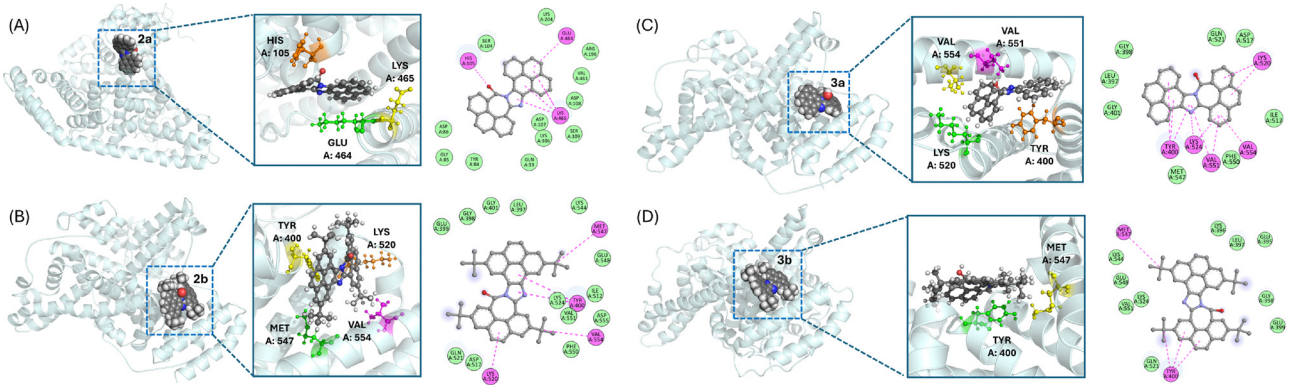

Fig. 14 Highest-scoring docking poses and 2D interaction diagrams of bovine serum albumin with (A) **2a**, (B) **2b**, (C) **3a**, and (D) **3b**.

2–3 orders of magnitude (see Table 2), mainly due to the lack of consideration of solvent–ligand interactions in the *in vacuo* docking analysis.

By binding with BSA, the imidazole unit of **3a** forms a hydrogen bond with Lys524, while the pyrene and phenanthrene moieties show alkyl–π stacking with Tyr400, Val551, Val554, and Lys520. For the **3b**–BSA complex, hydrogen bonding is absent due to increased steric bulkiness of *tert*-butyl groups. The alkyl–π interactions include those between a *tert*-butyl group and Met547 as well as the phenanthrene unit and Tyr400. The calculated binding energies are 9.94 kcal mol^{-1} for **3a** and 9.03 kcal mol^{-1} for **3b**, respectively.

Molecular dynamics simulations

Following the docking analysis, we performed molecular dynamics (MD) simulations to assess the dynamic stability of the highest-scoring fluorophore–BSA complexes under physiological conditions (pH 7.4, 298 K) in an aqueous solution containing 0.9% NaCl. Calculations were conducted by running the MD macro (md_run.mcr) implemented in the YASARA program and the results are summarized in Fig. 15.

The RMSD trajectories of the **2a**–BSA complex demonstrate high structural stability, with minimal deviations (<2 Å) throughout a simulation period of 40 ns. The MD results verify this complex as a stable system. In particular, the RMSF analysis reveals that the residues around the core binding site show limited flexibility (fluctuations <1.5 Å), while moderate fluctuations are observed in peripheral regions, consistent with the inherent dynamics of globular proteins. Notably, **2a** maintained stable interactions with the binding site, forming frequent hydrogen bonding interactions with BSA after 24 ns. Analysis of the simulation snapshots of **2a**–BSA at various time intervals shows that the ligand undergoes minor conformational changes and motions in the binding pocket. The MD analysis clearly demonstrates that **2a** can form a stable complex with BSA to retain good dynamic stability.

The RMSD trajectories of the **2b**–BSA complex also indicate structural stability of the protein backbone through the entire simulation period. However, notable fluctuations can be seen from the RMSD trace of the overall structure between 20 and 25 ns. Snapshot analysis shows significant ligand migration after 20 ns. Hydrogen bond analysis reveals that **2b** occasionally forms hydrogen bonding with the BSA substrate only within the first 6 ns. Compared with the **2a**–BSA complex, **2b** is more prone to diffusive motion upon binding with BSA. It is likely that the bulky and hydrophobic *t*-butyl groups facilitate the breaking and reformation of hydrogen bonds and other non-covalent interactions, allowing for easier ligand movement within the binding pocket. To further compare the dynamic stabilities of **2a**–BSA with **2b**–BSA, binding energies were calculated by analyzing the MD trajectories using the Boundary-Fasts method (md_analyzebindenergy macro) in the YASARA program. The results show average binding energies of −61.30 kJ mol^{-1} for **2a** and −95.71 kJ mol^{-1} for **2b**, and the

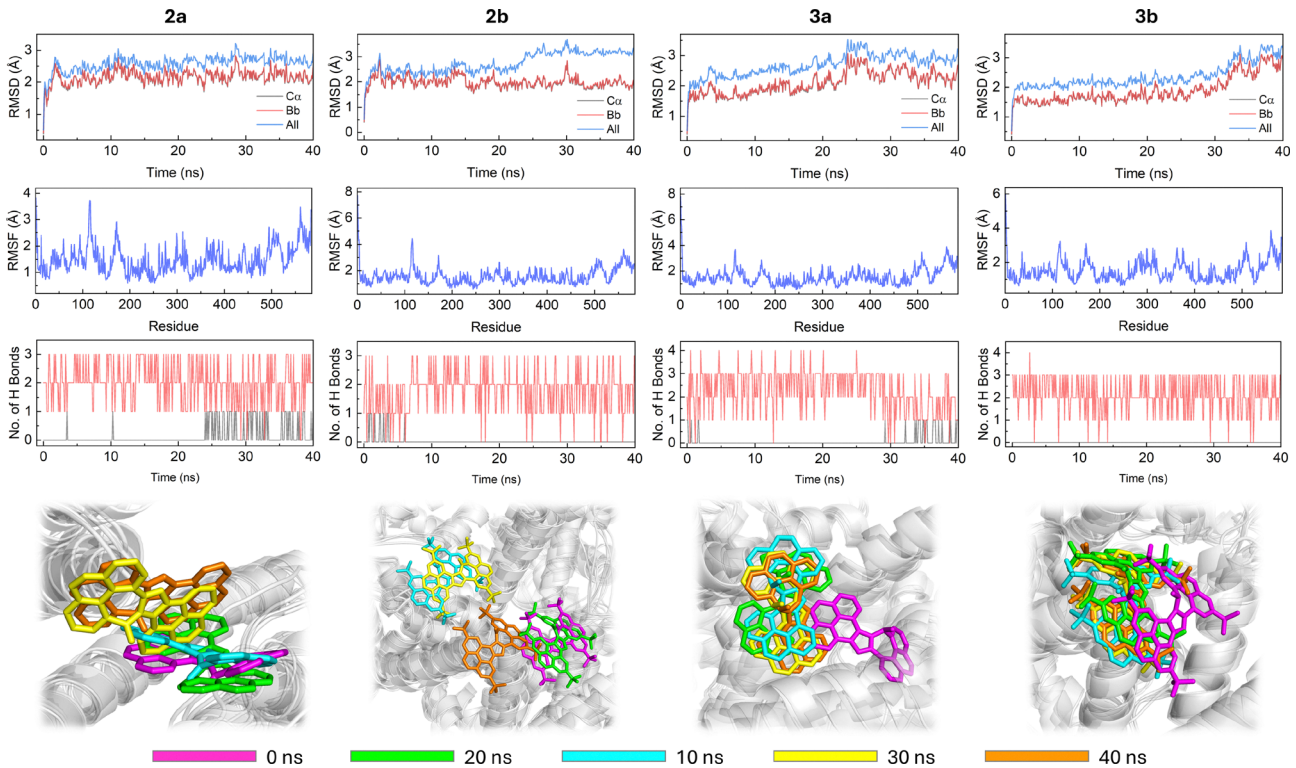

Fig. 15 Summary of MD simulation results for the complexes of BSA with **2a/b** and **3a/b**, respectively. Top row: RMSD traces for CA protein (C_α), backbone protein (Bb), and all-heavy atoms (all); second row: RMSF plots; third row: numbers of hydrogen bonds for ligand–protein (black traces) and ligand–solvent (red traces); fourth row: snapshots of fluorophore–BSA interactions taken at different time intervals of MD simulations.

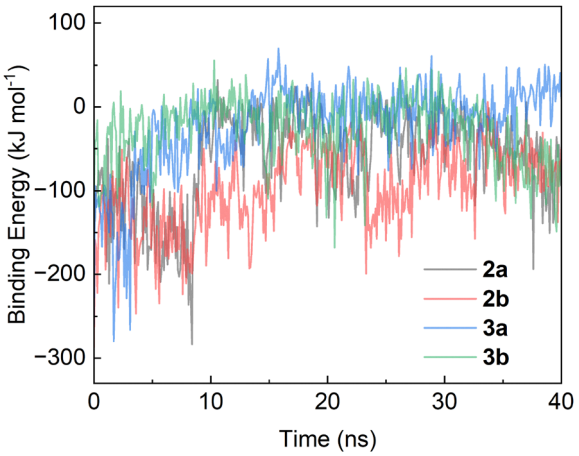

Fig. 16 Plots of binding energy calculated from the MD trajectories of BSA–fluorophore complexes using the BoundaryFasts method in YASARA.

detailed plots of MD-calculated binding energy as a function of simulation time are shown in Fig. 16. According to the YASARA algorithms, more positive energy values indicate stronger binding strengths. The MD analysis thus confirms that **2a** exhibits better dynamic stability as well as stronger affinity than **2b** in binding with BSA.

The complex of **3a** with BSA shows more structural fluctuations in both the protein backbone and the overall structure compared with **2a**–BSA. Snapshot analysis reveals that **3a** undergoes significant motion in the first 10 ns, migrating from the initial binding site to another site and then stabilizing there. This dynamic behavior indicates that the initial docking structure is metastable and the ligand tends to equilibrate into a more stable configuration within BSA as time evolves. Notably, hydrogen bonding between **3a** and BSA becomes more frequent after 30 ns of simulation, coinciding with the transition from the metastable to the more stable binding modes. The binding energy of **3a** calculated from its 40-ns MD trajectory is -21.93 kJ mol^{-1}, indicating a much stronger binding strength than **2a** and **2b**.

The **3b**–BSA complex exhibits structural fluctuations throughout the 40-ns MD simulation, as reflected by elevated RMSD values after 30 ns and more significant RMSF peaks for various residues. Of particular note is that **3b** forms no hydrogen bonds with BSA during the entire simulation period. Snapshot analysis reveals rapid ligand displacement from the initial binding site within the first 10 ns, followed by gradual equilibration. The calculated average binding energy of **3b**–BSA is -27.16 kJ mol^{-1}, which is slightly more negative than that of **3a**–BSA. The plot of binding energy of **3b**–BSA is similar to that of **3a**–BSA within the first 34 ns. After that, the trace of **3b**–BSA becomes more negative, indicating weaker binding strength.

Collectively, our MD simulations reveal two critical structure-binding relationships: (i) azepinone-centered fluorophores **2a** and **2b** show weaker binding with BSA than azepinol-based fluorophores **3a** and **3b** and (ii) fluorophores with *tert*-butyl peripheral groups show more diffusive motions in BSA than their unsubstituted analogues. In all cases, the fluorophores ultimately stabilize in hydrophobic pockets of BSA, an ideal microenvironment for preserving fluorescence quantum yield. The insights gained from MD simulations provide a deeper understanding of the observed long-wavelength fluorescence "turn-on" effect during titrations. The hydrophobic binding environment restricts molecular vibrations and non-radiative decay pathways that would otherwise quench emission.

It is worth remarking that both the docking and MD analyses predict that an unsubstituted fluorophore (**2a** or **3a**) binds with BSA more strongly than its *tert*-butyl-substituted analogue (**2b** or **3b**) does. This trend is in line with the general

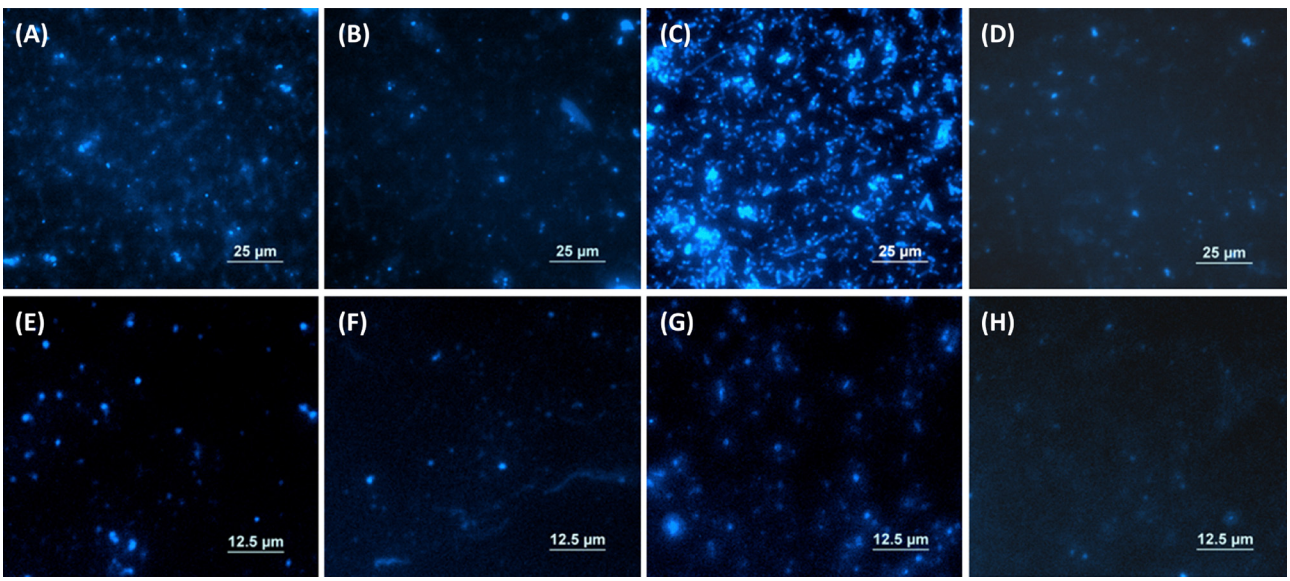

Fig. 17 Fluorescence microscopy images (λ_{ex} = 385 nm) of *Exiguobacterium* sp. N4-1P (top row) and *Alcanivorax venustensis* (bottom row) following 1-hour incubation with different fluorophores. Panels show bacteria treated with compounds **2a** (A) and (E), **2b** (B) and (F), **3a** (C) and (G), and **3d** (D) and (H).

expectation that the presence of bulky peripheral groups hinders the π-stacking and hydrogen bonding interactions between the fluorophore and binding residues of BSA. The experimentally determined binding properties (K_b, K_{SV}, and K_d^{obs}), however, all point to the opposite (see Table 2). Such discrepancies underscore the complexity of actual binding configurations in contrast to the simplified scenarios based on the highest-scoring docking configurations. More comprehensive experimental and simulation studies are therefore warranted to reconcile these inconsistencies.

Bacterial imaging

Following the BSA binding studies, we investigated the ability of the four fluorophores to label bacterial systems. Two model organisms representing distinct cell envelope architectures were selected: *Exiguobacterium* sp. N4-1P[60] (Gram-positive) and *Alcanivorax venustensis* (Gram-negative). Bacterial cultures were incubated with each fluorophore for varying time periods, with Fig. 17 demonstrating the fluorescence microscopic imaging results after 1 hour of incubation. Among the four fluorophores, azepinol-centered **3a** emerged as the most effective probe for Gram-positive *Exiguobacterium* sp. N4-1P, exhibiting superior cellular internalization and cell wall binding after 1-hour incubation, likely due to enhanced hydrogen-bonding interactions with the thick peptidoglycan layer.[61] Fluorescence intensity distribution analysis revealed preferential accumulation in intracellular regions rather than at cell wall boundaries.

Azepinone-based fluorophore **2a** showed measurable labeling capability (Fig. 17A and E), but its efficacy was significantly lower than that of **3a** (Fig. 17C and G). It is noteworthy that their *tert*-butyl substituted analogues **2b** (Fig. 17B and F) and **3b** (Fig. 17D and H) displayed limited penetration capacity, producing only sporadic fluorescent spots that failed to clearly delineate the bacterial morphology. This stark contrast highlights the critical influence of molecular bulk on bacterial labeling efficiency, where steric hindrance from *tert*-butyl groups appears to impede both cellular uptake and uniform distribution.[62,63]

Fluorescence imaging of Gram-negative *Alcanivorax venustensis* revealed relatively weak labeling across all fluorophores, with **3a** showing superior (though still modest) efficacy compared to its robust performance in labeling *Exiguobacterium* sp. N4-1P. This differential labeling capacity likely stems from fundamental differences in cell envelope architecture. Gram-negative bacteria possess an outer membrane containing lipopolysaccharides (LPS) and a thinner peptidoglycan layer, which may limit hydrogen-bonding interactions and create a penetration barrier for fluorophore internalization.[64]

It is worth noting that **3a** demonstrated unique versatility as the only compound capable of binding and internalization in both bacterial types. This superior activity suggests an optimal balance of amphipathicity (*i.e.*, possessing both hydrophobic and hydrophilic groups) and hydrogen bonding capacity, which enables traversal of diverse membrane structures.[65] Our findings point out that suitable modifications of the **Py-ImAz-Phen** structure can potentially lead to effective tuning of biological activities for improved cellular imaging.

Conclusions

In this study, we have systematically synthesized and characterized a new family of PAH fluorophores where pyrene and phenanthrene chromophores are fused together through either an imidazoazepinone or imidazoazepinol scaffold. These fluorophores differ in peripheral substitution and the π-conjugation patterns at the central azepine ring, yielding diverse electronic and photophysical properties. SCXRD analysis confirmed that modifications at the azepine core substantially alters molecular conformation, which, in turn, influences intermolecular interactions and solid-state packing behavior. UV-vis absorption and fluorescence spectroscopic studies revealed distinct solvatochromic and solvatofluorochromic properties. The azepinone derivatives (**2a** and **2b**) exhibited pronounced solvent-dependent fluorescence shifts, governed by a PLICT mechanism. In contrast, azepinol derivatives (**3a** and **3b**) showed minimal environmental sensitivity and significantly enhanced fluorescence quantum yields, attributable to their distorted geometry and lack of ICT character in the first excited state. EEM analyses further delineated the fundamental differences in excited-state dynamics between the planar and twisted fluorophore scaffolds.

Fluorescence titrations with a model protein, BSA, demonstrated that all four fluorophores form stable complexes with BSA, with different binding affinities and fluorescence responses. Notably, the azepinol-centered fluorophores **3a** and **3b** displayed strong fluorescence "turn-on" in the long-wavelength region due to an FRET-facilitated mechanism. Molecular docking and MD simulations provided deeper insights into structure-dependent binding modes and dynamic stability, highlighting the important roles of hydrogen bonding, alkyl–π stacking, and steric effects. Finally, the practical utility of these fluorophores in bioimaging was demonstrated by live-cell labeling of a Gram-positive (*Exiguobacterium* sp. N4-1P) and a Gram-negative (*Alcanivorax venustensis*) bacterium. Among the four fluorophores, azepinol-based **3a** emerged as a versatile probe with superior uptake and imaging capability, underlining the critical influence of molecular conformation and substituent effects on tuning the **Py-ImAz-Phen** framework for biological sensing and imaging. Overall, our studies paved a promising way for future development of **Py-ImAz-Phen** derivatives and their application in fluorescence sensing and bio-imaging.

Conflicts of interest

There are no conflicts to declare.

Data availability

Supplementary information (SI): optimized synthetic procedures, NMR and MS spectroscopic characterization studies of

2a, **2b**, **3a**, and **3b**. Detailed crystallographic data for **2a** (CCDC 2256234), **3a** (CCDC 2430295), and **2a**–BARF complex (CCDC 2430322). Stern–Volmer plots for the binding of BSA with **2a**, **2b**, **3a**, and **3b**. Detailed results of (TD)DFT calculations and MD simulations. See DOI: https://doi.org/10.1039/d5cp02942b.

CCDC 2256234, 2430322 and 2430295 contain the supplementary crystallographic data for this paper.[66a–c]

Acknowledgements

We thank the Natural Sciences and Engineering Research Council of Canada (NSERC) for funding support (RGPIN-2022-03782). Dr Jian-bin Lin of C-CART, Memorial University of Newfoundland, is acknowledged for collecting and solving the crystallographic data. The Digital Research Alliance of Canada is acknowledged for providing computational resources for the (TD)DFT calculations in this work. The Northern Region Persistent Organic Pollution Control (NRPOP) Laboratory at Memorial University is acknowledged for providing the two bacterial strains for our bacterial imaging studies.

References

1 X. Feng, J.-Y. Hu, C. Redshaw and T. Yamato, *Chem. – Eur. J.*, 2016, **22**, 11898–11916.
2 O. Ostroverkhova, *Chem. Rev.*, 2016, **116**, 13279–13412.
3 Q. Li, Y. Zhang, Z. Xie, Y. Zhen, W. Hu and H. Dong, *J. Mater. Chem. C*, 2022, **10**, 2411–2430.
4 J. Huang, J.-H. Su and H. Tian, *J. Mater. Chem.*, 2012, **22**, 10977–10989.
5 T. M. Figueira-Duarte and K. Mullen, *Chem. Rev.*, 2011, **111**, 7260–7314.
6 M. M. Islam, Z. Hu, Q. Wang, C. Redshaw and X. Feng, *Mater. Chem. Front.*, 2019, **3**, 762–781.
7 K. Ayyavoo and P. Velusamy, *New J. Chem.*, 2021, **45**, 10997–11017.
8 P. Srivastava, P. C. Fürstenwerth, J. F. Witte and U. Resch-Genger, *New J. Chem.*, 2021, **45**, 13755–13762.
9 X. Feng, X. Wang, C. Redshaw and B. Z. Tang, *Chem. Soc. Rev.*, 2023, **52**, 6715–6753.
10 P. J. Pacheco-Liñán, C. Alonso-Moreno, A. Ocaña, C. Ripoll, E. Garca-Gil, A. Garzón-Ruz, D. Herrera-Ochoa, S. Blas-Gómez, B. Cohen and I. Bravo, *ACS Appl. Mater. Interfaces*, 2023, **15**, 44786–44795.
11 L. Zhao, J. Li, L. Li and W. Hu, *J. Mater. Chem. C*, 2024, **12**, 13745–13761.
12 M. Tasior, D. Kim, S. Singha, M. Krzeszewski, K. H. Ahn and D. T. Gryko, *J. Mater. Chem. C*, 2015, **3**, 1421–1446.
13 A. Borissov, Y. K. Maurya, L. Moshniaha, W.-S. Wong, M. Żyła-Karwowska and M. Stepień, *Chem. Rev.*, 2021, **122**, 565–788.
14 A. Chevalier, *Org. Biomol. Chem.*, 2023, **21**, 7498–7510.
15 Y. Zhang, S.-L. Lai, Q.-X. Tong, M.-Y. Chan, T.-W. Ng, Z.-C. Wen, G.-Q. Zhang, S.-T. Lee, H.-L. Kwong and C.-S. Lee, *J. Mater. Chem.*, 2011, **21**, 8206–8214.
16 Y. Zhang, J.-H. Wang, G. Han, F. Lu and Q.-X. Tong, *RSC Adv.*, 2016, **6**, 70800–70809.
17 Y. Gao, N. Yi, Z. Ou, Z. Li, T. Ma, H. Jia, W. Xing, G. Yang and Y. Li, *Sens. Actuators, B*, 2018, **267**, 136–144.
18 J. Jayabharathi, P. Nethaji, V. Thanikachalam and R. Ramya, *ACS Omega*, 2019, **4**, 4553–4570.
19 X. Yang, Y. Zheng and L. Zheng, *J. Photochem. Photobiol., A*, 2022, **424**, 113575.
20 G. G. Dias, M. O. Rodrigues, E. R. Paz, M. P. Nunes, M. H. Araujo, F. S. Rodembusch and E. N. da Silva Júnior, *ACS Sens.*, 2022, **7**, 2865–2919.
21 A. Szlapa-Kula and S. Kula, *Energies*, 2023, **16**, 5194.
22 M. Zurnac, İ. Şener, M. Gür and N. Şener, *Luminescence*, 2023, **38**, 1690–1701.
23 B. Nemati Bideh, M. Moghadam, A. Sousaraei and B. Shahpoori Arani, *Sci. Rep.*, 2023, **13**, 2287.
24 D. Kumar, K. J. Thomas, C.-C. Lin and J.-H. Jou, *Chem. – Asian J.*, 2013, **8**, 2111–2124.
25 T. Jadhav, B. Dhokale, S. M. Mobin and R. Misra, *J. Mater. Chem. C*, 2015, **3**, 9981–9988.
26 S. Karthik, J. Ajantha, C. Nagaraja, S. Easwaramoorthi and T. Gandhi, *Org. Biomol. Chem.*, 2016, **14**, 10255–10266.
27 Z. A. Tabasi, J. C. Walsh, G. J. Bodwell, D. W. Thompson and Y. Zhao, *Cryst. Growth Des.*, 2020, **20**, 1681–1693.
28 V. Thanikachalam, U. Karunakaran, J. Jayabharathi and S. Thilagavathy, *J. Photochem. Photobiol. A*, 2021, **420**, 113489.
29 F. Liu, Z. Cheng, L. Wan, L. Gao, Z. Yan, D. Hu, L. Ying, P. Lu and Y. Ma, *Chem. Eng. J.*, 2021, **426**, 131351.
30 Y. Yan, Z. Cheng, Y. Xu, Z. Su, Y. Wang, X. He, Z. Zhao, F. Liu and P. Lu, *Adv. Funct. Mater.*, 2024, **34**, 2408550.
31 F. Liu, H. Liu, Y. Chen, X. He, Z. Cheng, X. Ma, X. Qiao, D. Ma and P. Lu, *CCS Chem.*, 2025, 1–13.
32 F. Shahrokhi and Y. Zhao, *Org. Lett.*, 2019, **21**, 9306–9310.
33 M. J. Alonso-Navarro, A. Harbuzaru, M. Martnez-Fernández, P. P. Camero, J. T. L. Navarrete, M. M. Ramos, R. P. Ortiz and J. L. Segura, *J. Mater. Chem. C*, 2021, **9**, 7936–7949.
34 H. Fang, Y. Chen, Z. Jiang, W. He and Z. Guo, *Acc. Chem. Res.*, 2023, **56**, 258–269.
35 H. Liu, G. Jiang, G. Ke, T.-B. Ren and L. Yuan, *ChemPhotoChem*, 2024, **8**, e202300277.
36 J. Yang, Z. Xu, L. Yu, B. Wang, R. Hu, J. Tang, J. Lv, H. Xiao, X. Tan and G. Wang, *et al.*, *Angew. Chem. Int. Ed.*, 2024, **63**, e202318800.
37 Y. Zhang, Y. Huang, G. Yang, H. Xin, K. Li, L. Wang, S. Gu, B. Ren, S. Zhao and D. Cao, *J. Hazard. Mater.*, 2025, 137452.
38 A. Guijarro, J. A. Vergés, E. San-Fabián, G. Chiappe and E. Louis, *Chem. Phys. Chem.*, 2016, **17**, 3548–3557.
39 E. M. Cabaleiro-Lago and J. Rodriguez-Otero, *ACS Omega*, 2018, **3**, 9348–9359.
40 K. Carter-Fenk and J. M. Herbert, *Phys. Chem. Chem. Phys.*, 2020, **22**, 24870–24886.
41 E. v Lippert, *Ber. Bunsenges. Phys. Chem.*, 1957, **61**, 962–975.
42 N. Mataga, Y. Kaifu and M. Koizumi, *Bull. Chem. Soc. Jpn.*, 1956, **29**, 465–470.

43 K. Zachariasse, M. Grobys, T. Von Der Haar, A. Hebecker, Y. V. Il'Ichev, O. Morawski, I. Rückert and W. Kühnle, *J. Photochem. Photobiol., A*, 1997, **105**, 373–383.
44 C. Zhong, *Phys. Chem. Chem. Phys.*, 2015, **17**, 9248–9257.
45 G. Haberhauer, R. Gleiter and C. Burkhart, *Chem. – Eur. J.*, 2016, **22**, 971–978.
46 G. Haberhauer, *Chem. – Eur. J.*, 2017, **23**, 9288–9296.
47 R. L. Martin, *J. Chem. Phys.*, 2003, **118**, 4775–4777.
48 S. Karthik, J. Ajantha, S. Easwaramoorthi and T. Gandhi, *New J. Chem.*, 2020, **44**, 9530–9539.
49 X. Xu, J. Hu, H. Xue, Y. Hu, Y.-N. Liu, G. Lin, L. Liu and R.-A. Xu, *Int. J. Biol. Macromol.*, 2023, **253**, 126914.
50 S. Behera, P. Mohanty, P. P. Dash, P. Mohapatra, L. Shubhadarshinee, R. Behura, A. K. Barick, P. Mohapatra and B. R. Jali, *Biointerface Res. Appl. Chem.*, 2023, **13**, 555.
51 A. Bujacz, *Acta Crystallogr., Sect. D: Biol. Crystallogr.*, 2012, **68**, 1278–1289.
52 N. Tayeh, T. Rungassamy and J. R. Albani, *J. Pharm. Biomed. Anal.*, 2009, **50**, 107–116.
53 B. K. Paul and N. Guchhait, *Photochem. Photobiol. Sci.*, 2011, **10**, 980–991.
54 J. R. Lakowicz, *Principles of Fluorescence Spectroscopy*, Springer, New York, NY, 3rd edn, 2006.
55 I. V. Govor, A. L. Tatarets, O. M. Obukhova, E. A. Terpetschnig, G. Gellerman and L. D. Patsenker, *Methods Appl. Fluoresc.*, 2016, **4**, 024007.
56 S. Bhuin, S. Halder, S. K. Saha and M. Chakravarty, *RSC Adv.*, 2021, **11**, 1679–1693.
57 A. Jahanban-Esfahlan, A. Ostadrahimi, R. Jahanban-Esfahlan, L. Roufegarinejad, M. Tabibiazar and R. Amarowicz, *Int. J. Biol. Macromol.*, 2019, **138**, 602–617.
58 O. Trott and A. J. Olson, *J. Comput. Chem.*, 2010, **31**, 455–461.
59 E. Krieger and G. Vriend, *Bioinformatics*, 2014, **30**, 2981–2982.
60 Q. Cai, B. Zhang, B. Chen, Z. Zhu and Y. Zhao, *RSC Adv.*, 2017, **7**, 42699–42708.
61 N. Nagarajan, G. Vanitha, D. A. Ananth, A. Rameshkumar, T. Sivasudha and R. Renganathan, *J. Photochem. Photobiol., B*, 2013, **127**, 212–222.
62 M. Baudoin, A. Chouquet, M. Nguyen, A. Zapun, B. Pérès, C. Morlot, C. Durmort and Y.-S. Wong, *RSC Adv.*, 2024, **14**, 33133–33142.
63 J. Hira, M. J. Uddin, M. M. Haugland and C. S. Lentz, *Mol.*, 2020, **25**, 4949.
64 G. Zhang, T. C. Meredith and D. Kahne, *Curr. Opin. Microbiol.*, 2013, **16**, 779–785.
65 J. Ouyang, Y. Sheng and W. Wang, *Cells*, 2022, **11**, 4016.
66 (*a*) CCDC 2256234: Experimental Crystal Structure Determination, 2026, DOI: 10.5517/ccdc.csd.cc2fqsrq; (*b*) CCDC 2430322: Experimental Crystal Structure Determination, 2026, DOI: 10.5517/ccdc.csd.cc2mkyhn; (*c*) CCDC 2430295: Experimental Crystal Structure Determination, 2026, DOI: 10.5517/ccdc.csd.cc2mkxmr.